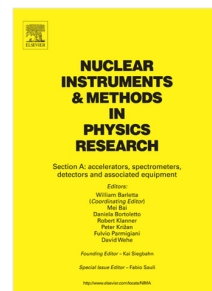


Journal Pre-proof

The CLAS12 Backward Angle Neutron Detector (BAND)

E.P. Segarra, F. Hauenstein, A. Schmidt, A. Beck, S. May-Tal Beck,
R. Cruz-Torres, A. Denniston, A. Hrnjic, T. Kutz, A. Nambrath,
J.R. Pybus, O. Hen, K. Price, C. Fogler, T. Hartlove, L.B. Weinstein,
I. Vega, M. Ungerer, H. Hakobyan, W. Brooks, E. Piasetzky, E. Cohen,
M. Duer, I. Korover, J. Barlow, E. Barriga, P. Eugenio, A. Ostrovidov



PII: S0168-9002(20)30753-1
DOI: <https://doi.org/10.1016/j.nima.2020.164356>
Reference: NIMA 164356

To appear in: *Nuclear Inst. and Methods in Physics Research, A*

Received date: 5 May 2020
Revised date: 23 June 2020
Accepted date: 9 July 2020

Please cite this article as: E.P. Segarra, F. Hauenstein, A. Schmidt et al., The CLAS12 Backward Angle Neutron Detector (BAND), *Nuclear Inst. and Methods in Physics Research, A* (2020), doi: <https://doi.org/10.1016/j.nima.2020.164356>.

This is a PDF file of an article that has undergone enhancements after acceptance, such as the addition of a cover page and metadata, and formatting for readability, but it is not yet the definitive version of record. This version will undergo additional copyediting, typesetting and review before it is published in its final form, but we are providing this version to give early visibility of the article. Please note that, during the production process, errors may be discovered which could affect the content, and all legal disclaimers that apply to the journal pertain.

© 2020 Elsevier B.V. All rights reserved.

The CLAS12 Backward Angle Neutron Detector (BAND)

E.P. Segarra, F. Hauenstein^{1,*}, A. Schmidt², A. Beck³, S. May-Tal Beck³, R. Cruz-Torres, A. Denniston, A. Hrnjic, T. Kutz, A. Nambrath, J.R. Pybus, O. Hen

Massachusetts Institute of Technology, Cambridge, Massachusetts 02139, USA

K. Price⁴, C. Fogler, T. Hartlove, L.B. Weinstein

Old Dominion University, Norfolk, Virginia 23529, USA

I. Vega, M. Ungerer, H. Hakobyan, W. Brooks

Universidad Técnica Federico Santa María, Casilla 110-V Valparaíso, Chile

E. Piasetzky, E. Cohen, M. Duer

School of Physics and Astronomy, Tel Aviv University, Tel Aviv 69978, Israel

I. Korover

Nuclear Research Center Negev, Be'er Sheva 84190, Israel

J. Barlow, E. Barriga, P. Eugenio, A. Ostrovidov

Florida State University, Tallahassee, Florida 32306, USA

Abstract

The Backward Angle Neutron Detector (BAND) of CLAS12 detects neutrons emitted at backward angles of 155° to 175° , with momenta between 200 and 600 MeV/c. It is positioned 3-m upstream of the target, consists of 18 rows and 5 layers of 7.2-cm by 7.2-cm scintillator bars, and read out on both ends by PMTs to measure time and energy deposition in the scintillator layers. Between the target and BAND there is a 2-cm thick lead wall followed by a 2-cm veto layer to suppress gammas and reject charged particles.

This paper discusses the component-selection tests and the detector assembly. Timing calibrations (including offsets and time-walk) were performed using a novel pulsed-laser calibration system, resulting in time resolutions better than 250 ps (150 ps) for energy depositions above 2 MeV (5 MeV). Cosmic rays and a variety of radioactive sources were used to calibrate the energy response of the detector. Scintillator bar attenuation lengths were measured. The time resolution results in a neutron momentum reconstruction resolution, $\delta p/p < 1.5\%$ for neutron momentum $200 \leq p \leq 600$ MeV/c. Final performance of the BAND with CLAS12 is shown, including electron-neutral particle timing spectra and a discussion of the off-time neutral contamination as a function of energy deposition threshold.

Keywords: CLAS12; time of flight; plastic scintillator; ultrafast neutrons

*Corresponding Author

Email address: hauenst@jlab.org (F. Hauenstein)

¹Also at: Old Dominion University, Norfolk, Virginia 23529, USA

²Current address: George Washington University, Washington, D.C. 20052, USA

³Also at: Nuclear Research Center Negev, Be'er Sheva 84190, Israel

⁴Current address: Institut de Physique Nucléaire, IN2P3-CNRS,

1. Introduction

CLAS12 (12-GeV CEBAF Large Acceptance Spectrometer) [1] in Hall B of the Thomas Jefferson National Accelerator Facility (JLab) is a multi-purpose spectrometer used to detect charged and neutral particles emit-

F-91406 Orsay, France

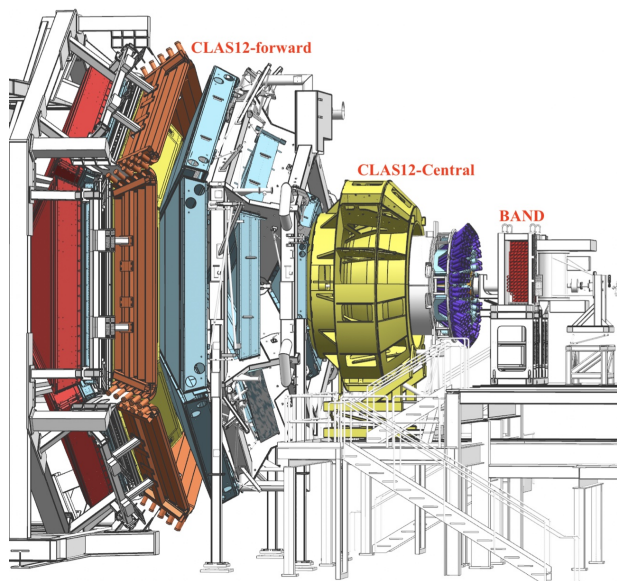


Figure 1: CLAS12 and BAND in Hall B at Jefferson Lab. The electron beam is incident from the right side. BAND is marked in red. The overall detector system is roughly 20 m in scale along the beam axis.

ted in high-energy electron scattering reactions. Tagged deep inelastic scattering studies require the detection of backward-angle recoil neutrons with momenta above 200 MeV/c [2]. This is achieved by a combination of the Central Neutron Detector (CND) [3] and the Backward Angle Neutron Detector (BAND). The CND covers angles from 40° to 120° while BAND covers from 155° to 175°.

BAND was designed to measure neutrons with momenta of 200 – 600 MeV/c, with an average detection efficiency of 35%, and with a momentum reconstruction resolution better than 1.5%. The detector is based on scintillator bars with PMT readout on both bar ends. BAND was installed in January 2019 and has since taken data in coincidence with CLAS12. Fig. 1 shows a drawing of BAND located upstream of CLAS12 in Hall B.

This paper describes the design, operation and calibration of the BAND. Section 2 presents the required time resolution, efficiency and geometry, the resulting design and layout, the selection of detector components, and results from comparative measurements of different PMTs and magnetic shields. Section 3 presents the performance of the detector after its installation in Hall B. It describes cosmic-ray and laser calibrations [4] as well as the measured time-of-flight (ToF) resolutions and neutron-photon separation from 10.6-GeV electron-deuteron data. Section 4 summarizes the results.



Figure 2: BAND and its close surroundings: the cryotarget and beam line components (cyan), BAND (red), the central detector region of CLAS12 (blue), the space frame (black), and the central detector support cart (grey). The beam is coming from the left side. The target is located at the center of the CLAS12 central detector.

2. Design of the backward angle neutron detector

The major considerations for the BAND design were the constraints on geometry and areal coverage in Hall B, the time-of-flight resolution required, and neutral particle identification. To achieve the physics of interest in BAND [2], neutron ToF resolutions below 300 ps at an energy deposition threshold of ~ 2 MeVee (MeV-electron-equivalent) are required. This threshold is later optimized using neutron signal-counts-above-background, measured ToF resolutions and neutron efficiencies as a function of minimum energy deposition. Neutral particles are identified by using a thin 2-cm veto layer for charged-particle identification between the target and the first active layer of BAND. Photons are suppressed by a 2-cm thick lead wall placed downstream of the veto layer. Neutron-photon discrimination is achieved via ToF relative to the electron scattering time measured by CLAS12. Out-of-time random neutron and photon contamination in a signal region can be reduced, relative to the signal strength, by optimizing the minimum energy deposition of particles in the bars (see discussion in *Neutron identification*).

The following subsections describe the BAND geometry, the individual components, including the bench measurements that informed their selection, the photon shielding, the laser calibration system, the electronics and data acquisition, and the final assembly of the detector.

2.1. Geometry

The design of the BAND geometry balanced the goal of maximizing acceptance for backward angle neutrons

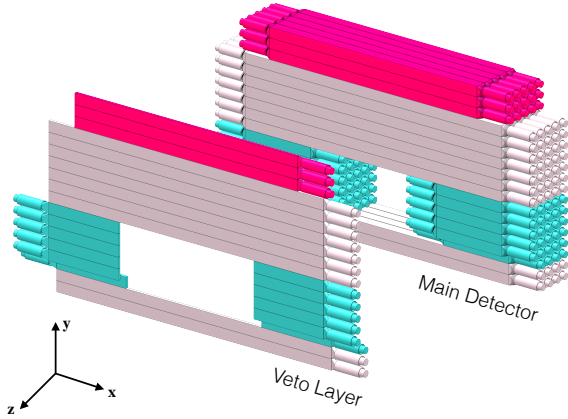


Figure 3: BAND design of bars in the main detector and the veto layer. The 164-cm long bars are shown in red, the 202-cm bars in white and the short, 51-cm bars in cyan. The position of the PMTs for each bar is also shown. The beam direction corresponds to the z -axis.

with the space constraints in hall (see Fig. 2). BAND was designed to cover the region between the Central Detector and the target support, where the flight path of the neutrons had minimal material obstruction. In order to be installed on the support cart for the central tracking detectors, BAND had to be lowered down through an existing opening in the CLAS12 support scaffolding (referred to as the space frame, shown in black in Fig. 2). This required that BAND fit within a box 3-m wide, 1.5-m high, and 1-m deep, and include a hole in the middle for the beam pipe.

To maximize the active detector volume within these constraints, we chose to use rectangular scintillator bars stacked (in x - y), perpendicular to the beam direction (z), see Fig. 3. The cross section of each scintillator bar determines our position granularity in y , z (vertical and longitudinal directions relative to the beam pipe), and should be comparable to our time-resolution-dependent position resolution along the bar (in x). Given our time-resolution specification of 300 ps (discussed below), 7.2 cm by 7.2 cm scintillator bars were chosen to optimize fiducial volume, granularity, and cost.

The active detector area (excluding the veto layer) consists of 116 scintillator bars, arranged in 5 z -layers with 18 vertically stacked rows of bars. The arrangement of the bars is shown in Fig. 3. The bottom three rows each have only four layers due to obstructions from the cart below BAND (see grey cart in Fig. 2).

Three different bar lengths are used: 15 bars of length 164 cm, 43 bars of length 202 cm, and 58 bars of length 51 cm. The shorter bars were used in the vicinity of the beam pipe. All bars have light guides attached to

Table 1: Parameters for bars and PMTs for the different BAND sectors and layers.

	Dimensions ($w \times h$)	PMT
Sector 1, $L = 164$ cm		
Layer 1 – 5	7.2×7.2 cm ²	R7724
Layer 6	2×7.2 cm ²	9954KB
Sector 2, $L = 202$ cm		
Layer 1 – 5	7.2×7.2 cm ²	R7724
Layer 6	2×7.2 cm ²	9954KB
Sector 3 / 4, $L = 51$ cm		
Layer 1 – 4	7.2×7.2 cm ²	9214KB
Layer 5	7.2×7.2 cm ²	R7724
Layer 6	2×7.2 cm ²	9954KB
Sector 5, $L = 202$ cm		
Layer 1 – 4 ^a	7.2×7.2 cm ²	R7724
Layer 6	2×7.2 cm ²	9954KB

both sides, and the bars are read out by 51 mm PMTs. The PMTs are either Hamamatsu R7724 [5] or Electron Tubes (ET) 9214KB [6] (see Table 1).

The veto layer, which is installed on the downstream face of BAND (i.e., between BAND and the target), consists of 24 scintillator bars with a cross section of 2 cm by 7.2 cm. The veto bars have the same lengths as the corresponding BAND bars, such that the whole downstream surface is covered by the veto, see Fig. 3. Each veto bar is only read out on one side by a single ET 9954KB [7] 51 mm PMT.

Each bar has an assigned sector and layer number. The layer number corresponds to the position along the beam line (in z) starting from upstream (1) to downstream (5) for the active area and (6) for the veto bars. The sector numbering follows from top to bottom. Sector 1 consists of three rows of 164-cm long bars (red bars in Fig. 3). Sector 2 has seven rows of 202-cm long bars, below Sector 1. Sector 5 also consists of the 202-cm long bars, two rows on the bottom of the detector. The white bars in Fig. 3 show the locations of Sectors 2 and 5 in each layer. The short 51-cm bars to the left of the beam hole (negative x) are in Sector 3, while the ones on the right side (positive x) are in Sector 4 (both are shown in cyan in Fig. 3). Table 1 summarizes the geometry parameters and PMTs for each sector and layer.

2.2. Components

The timing resolution of the scintillator bars is affected by many factors, and each component was optimized considering both cost and design constraints.

^aLayer 5 is missing due to obstructions from the central detector support cart below BAND

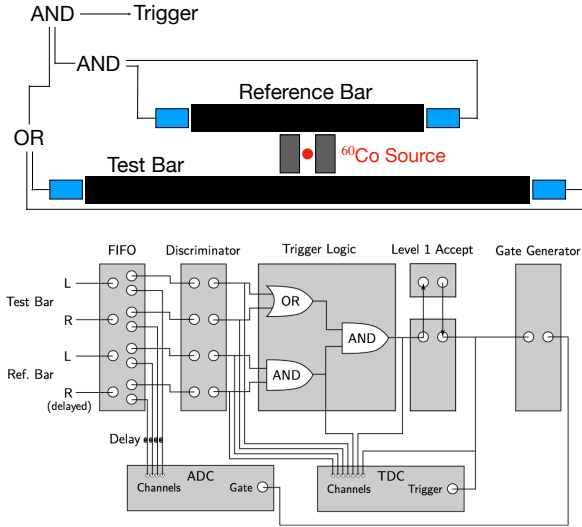


Figure 4: Schematic of the bench test setup (top) and its read-out system (bottom) to measure PMT time resolutions.

127 We selected Bicron BC-408 [8] scintillant for its light
 128 output, time response and attenuation length. The bulk
 129 attenuation length of 380 cm is much longer than the
 130 length of the BAND bars. To enhance reflectivity, we
 131 wrapped each bar with 3M Enhanced Specular Reflector
 132 foils [9]. In order to select the optimal PMTs and
 133 thickness of magnetic-shields, we bench-tested a variety
 134 of options described in the following text.

135 2.2.1. Bench Measurements

136 Bench measurements were used to guide the PMT
 137 and magnetic shielding selection. A diagram of our test
 138 setup and electronics is shown in Fig. 4, featuring a
 139 coincidence setup between a “test” scintillator bar and a
 140 “reference” scintillator bar. Each bar has two PMTs
 141 coupled to its ends; the test bar has the PMTs whose
 142 time resolution we wish to study. Both bars are wrapped
 143 in an optical reflector, and placed in a dark-box. The
 144 reference bar was kept fixed during all measurements. Five
 145 different 51-mm PMTs were tested (see Table 2, [10],
 146 and [6]), assembled on 200- to 250-cm long bars.

147 The signal for our measurement is given by a ^{60}Co
 148 source which is placed between the two bars. The ^{60}Co
 149 source yields two γ rays with energies of 1.17 and 1.33
 150 MeV. The two γ -rays were collimated by two lead
 151 bricks to ensure they each hit a specific location along
 152 each bar, allowing us to study individual PMT time
 153 resolution and measured energy as a function of hit
 154 location.

155 Measurements with different ^{60}Co source locations

Table 2: Bench test configurations. Length refers to the length of the scintillator bar. σ is the time resolution for 2-MeV central-equivalent energy deposit in the middle of the bar extrapolated from data. The 9214KB PMT [6] is manufactured by ET-Enterprises and the other PMTs are manufactured by Hamamatsu [10].

PMT	Length (cm)	σ (ps)
R7724	200	~ 240
R7724-100	250	~ 210
R13089	250	~ 210
R13435	200	~ 310
9214KB	200	~ 260

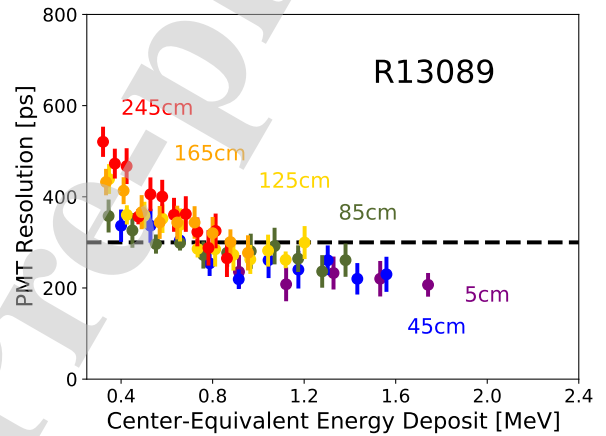


Figure 5: PMT time resolution as a function of center-equivalent energy deposit for different placements of the ^{60}Co source along the bar for Hamamatsu R13089 PMT. The labels indicate the distance of the source to the PMT.

156 were combined by using the measured attenuation in
 157 the bar to convert the energy measured by the PMT
 158 to the “center-equivalent energy deposit,” the energy
 159 that would have been deposited at the center of the bar
 160 to give the same measured energy. For example, by
 161 placing the source close to one PMT one can achieve
 162 a center-equivalent energy deposit significantly greater
 163 than the 1 MeV ^{60}Co Compton edge.

164 Fig. 5 shows the PMT time resolution as a function of
 165 center-equivalent energy deposited for different source
 166 placements. Each individual data set explores the re-
 167 sponse of the PMT over the entire Compton distribution
 168 for a single source placement. Since the individual data
 169 sets are consistent within error bars, the measurements
 170 were combined to cover a center-equivalent energy de-
 171 position range up to 1.8 MeV.

172 Fig. 6 shows the measured single-PMT time resolution
 173 for the different test configurations. The lines indi-
 174 cate fits to data extrapolated beyond 1.8 MeV. All

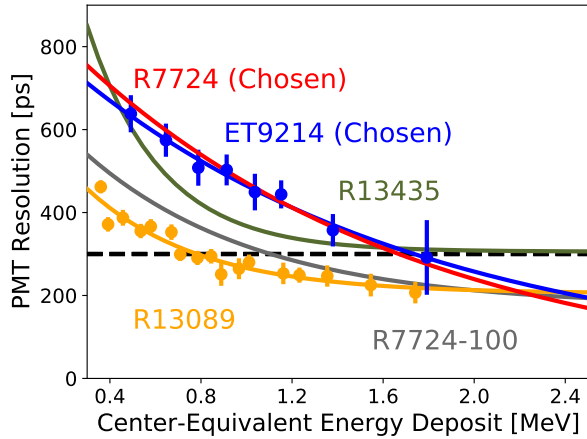


Figure 6: Single-PMT time resolution as a function of center-equivalent energy deposit for the five PMTs tested. For each PMT, data, such as that of Fig. 5, are combined to a single set and weighted averages are taken to reduce error given the density of points. The lines are fits to data (only the blue and yellow data points are shown). The functional form used, $\sigma_{PMT} = ae^{-bE_{dep}} + c$, reflects that at sufficiently high energy deposition, PMT resolution becomes constant. At 2 MeV energy deposition all PMTs except R13435 achieve a time resolution below 300 ps.

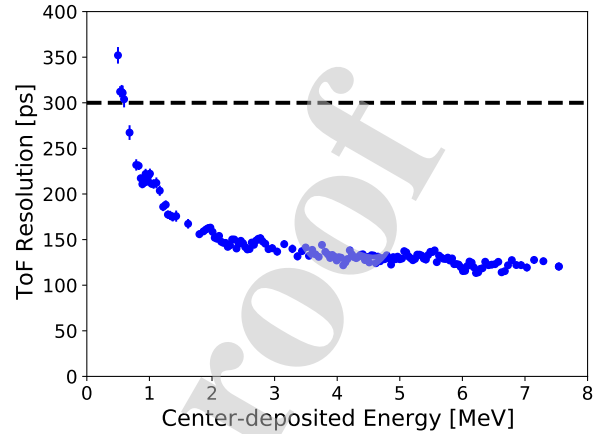


Figure 7: Time resolution as a function of center-deposited energy for one bar with R7724 PMTs using the BAND laser system after installation. The energy deposition is the geometric mean of both PMTs at the end of the bar, and is corrected for attenuation effects. The deposition is in the center of the bar due to the installation of the fiber there.

175 PMTs except the R13435 met the timing-resolution de-
 176 sign specification of 300 ps at 2-MeV energy deposi-
 177 (see Table 2). To reduce costs, a combination of Hama-
 178 matsu R7724 [5] and Electron Tube 9214KB [6] PMTs
 179 for BAND were selected. For the veto layer, available
 180 Electron Tube 9954KB PMTs were used. See Table 3
 181 for details of the selected PMTs.

182 After BAND was assembled and installed, the time
 183 resolution of each bar was measured using the laser cal-
 184 ibration system (see Sec. 2.4 and [4]). The time resolu-
 185 tion as a function of the energy deposit in the center of
 186 the bar is shown in Fig. 7 for a representative 202-cm
 187 bar with R7724 PMTs. The resolution is below 150 ps
 188 from 2 to 8 MeV center-deposited energy, indicating the
 189 good performance of the bars and PMTs. One should
 190 note that Fig. 7 is the bar ToF resolution, while 6 is the
 191 PMT resolution. In Fig. 7, the energy deposition is mea-
 192 sured from both PMTs (reconstructed as the geometric
 193 mean and corrected for attenuation).

194 2.2.2. Light Guides

195 The light guide design was constrained by the avail-
 196 able space, the sizes of the scintillator bars and PMTs,
 197 and the length of the mu-metal shielding. The design
 198 utilizes a modified Winston cone to optimize light col-
 199 lection by concentrating light from a large area at the
 200 scintillator onto a smaller active area of the photomul-
 201 tiplier. CAD drawings of the light guides for the main

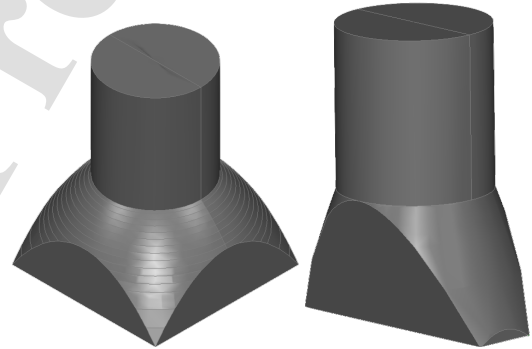


Figure 8: CAD drawing of the light guides for the main detector (left) and the veto bars (right). The top parts are connected to the PMTs while the lower parts are connected to the bars.

202 detector and the veto bars are shown in Fig. 8. In to-
 203 tal, they are 8.9 cm long. Each light guide has a 4.9-cm
 204 long cylindrical section with a 4.6-cm diameter, which
 205 is connected to the active photocathode area of the 51-
 206 mm diameter PMTs. The cylindrical length allows for
 207 the magnetic field shielding to extend more than 51 mm
 208 (i.e., more than a PMT diameter) beyond the photocath-
 209 ode (see next section). The other end of the light guide
 210 matches the cross section of the scintillator. The light
 211 guide is glued to the scintillator bar with a DYMAX
 212 UV curing glue [11] and attached to the PMT with MO-
 213 MENTIVE RTV615 silicone rubber compound [12].
 214 The light guides were designed, optimized, and man-
 215 ufactured by Florida State University.

Table 3: Properties of the PMTs used in BAND.

	R7724 [5]	9214KB [6]	9954KB [7]
Company	Hamamatsu	ET	ET
Diameter	51 mm	51 mm	51 mm
Dynode stages	10	12	12
Spectral response	300 – 650 nm	290 – 630 nm	290 – 680 nm
Max. wavelength emission	420 nm	350 nm	380 nm
Quantum eff. maximum	26%	30%	28%
Gain	3.3×10^6	3.0×10^7	1.8×10^7
Max. anode current rating	200 μ A	100 μ A	100 μ A
Anode dark current	6 nA	4 nA	8 nA
Anode pulse rise time	2.1 ns	2.0 ns	2.0 ns
Electron transit time	29 ns	45 ns	41 ns

2.2.3. PMT Magnetic shielding

The fringe field of the CLAS12 solenoid magnet [13] is between 20 and 120 G at the location of BAND, requiring all PMTs to have magnetic shielding. The transverse field (perpendicular to the axis of the PMT) in the PMT region ranged from 10 to 110 G and the longitudinal field ranged from 10 to 50 G.

A dedicated test stand was used to examine different thicknesses of passive magnetic shielding. Two 56-turn Helmholtz coils, with a radius of 0.5 m, separated by 1 m, were constructed. A prototype detector was also used, consisting of a 2-cm thick, 5-cm diameter scintillator disc, coupled to two 7-cm long, 5-cm diameter cylindrical acrylic light guides and two PMTs. The detector was light-proofed with Tedlar® and stabilized on a simple plastic stand at the center of the Helmholtz coils.

As a baseline, responses to ^{90}Sr and ^{137}Cs sources were measured with zero magnetic field and no shielding. The sources were placed either 0 or 5 cm away from the scintillant. PMT event rates, time differences between the left and right PMT signals, and peak energies were measured at nominal operating voltages.

The same quantities were subsequently measured with different shielding configurations at different longitudinal and transverse magnetic fields, up to 80 G (limited by heat dissipation in the Helmholtz coils).

Mu-metal shielding of thicknesses of 0.9, 1.5, 1.8, 2.4 and 3 mm were tested, as well as two soft-iron pipes. The magnetic field, amount of detector covered by the shielding, the thickness of the shielding, and the angle of the detector to the field were all varied.

In Fig. 9, the event rate from a ^{90}Sr source as a function of magnetic field strength is shown for different thickness of mu-metal shields and a reference measurement without any shield. The shield was positioned to

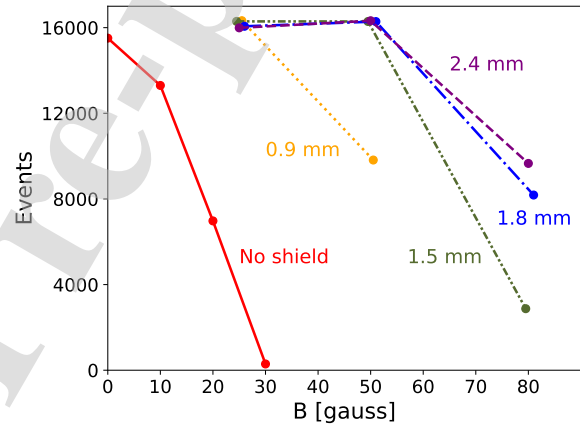


Figure 9: Magnet shielding test results with a ^{90}Sr source, a longitudinal field. The shields were placed to cover 5 cm beyond the PMT photocathode. Event rates with increasing field and no shielding are shown in red. Results with 0.9, 1.5, 1.8, and 2.4 mm mu-metal thickness are shown in yellow, green, blue, and purple, respectively.

cover 5 cm beyond the photocathode. The longitudinal magnetic field degraded the PMT performance the most. While the 1.5-mm mu-metal shield was not sufficient, the 1.8-mm mu-metal shield maintained PMT performance up to 80 G. The soft-iron pipes performed worse than the 1.5-mm mu-metal (not shown in Fig. 9). The magnetic shields performed best when they extended 5 cm (one diameter) beyond the PMT photocathode. In order to be conservative, 2.6-mm thick mu-metal shields were selected.

2.2.4. PMT and bar quality test measurements

Before the final assembly of BAND (see Section 2.6), all PMTs and bars have been tested for quality assurance. These measurements were conducted with a picosecond pulsed UV-LED.

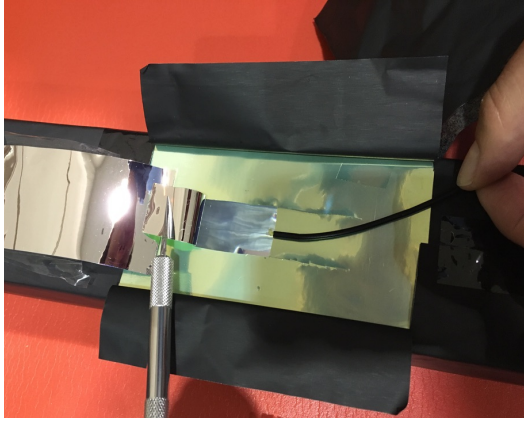


Figure 10: Connection of a fiber to bar after UV-cure gluing. The fiber is positioned in the center of the bar and is covered by both layers of wrapping material, ESR [9] and Thorlabs Aluminium foil [14].

267 The test setup for each PMT had a 6.4-cm long scin-
 268 tillator disc attached between the LED and the PMT in-
 269 side of a light-tight dark box. Gains and time resolu-
 270 tions for each PMT were measured. The PMTs were
 271 then matched in pairs to be then glued to a bar. Pairs
 272 were determined by minimizing gain different and time
 273 resolution difference between the PMTs of a pair.

274 For each bar the attenuation length was measured by
 275 moving the LED pulser along the bar. This was done
 276 without a wrapping material around the bar and with no
 277 light guides attached, in a light tight black-box. The
 278 bars with the worst attenuation length were selected as
 279 back-up bars.

280 2.3. Lead shielding

281 To minimize background from backward-going pho-
 282 tons, a lead wall was installed on the downstream face
 283 of BAND (between the CLAS12 target and BAND).
 284 This lead wall consists of individual 2-cm thick blocks
 285 stacked in front of the veto layer. Each block is covered
 286 on both sides with an aluminum layer to safely handle.
 287 The lead wall can be seen in the final assembly pho-
 288 tographs shown in Fig. 13.

289 2.4. Laser Calibration system

290 A UV laser system to calibrate BAND and monitor its
 291 performance was implemented during data-taking. The
 292 design and performance of the system is fully described
 293 in Ref. [4].

294 The main component of the system is a picosecond
 295 pulsed diode laser (Teem Photonics STV-01E-140, [15])
 296 with a wavelength of 355 nm. The laser can be triggered

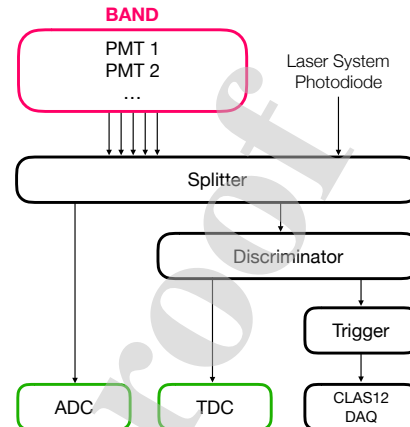


Figure 11: Electronic schematic of the BAND read-out. Every PMT signal is split and ADC and TDC information are obtained. Additional outputs of the discriminators are used to create single bar and cosmic-laser triggers from BAND.

297 externally between 10–4000 Hz. The light is only trans-
 298 ported within fibers. Further components of the system
 299 are a mode scrambler, a 90:10 splitter whose outputs
 300 are connected to a reference photodiode (10% output)
 301 and a variable optic attenuator [16] (90% output). The
 302 attenuator allows to vary the pulse intensity sent to the
 303 detector. It is connected to a custom SQS Vláknová Op-
 304 tika 1×400 splitter which distributes the light to every
 305 bar of BAND.

306 Each bar has an optical fiber glued to its center with
 307 UV-curable glue (see Fig. 10). We used an exposed fiber
 308 for the fiber-scintillant connection since it was a stable,
 309 reliable and easy option. The other end of the fiber is
 310 connected to the splitter through a patch panel attached
 311 to the BAND frame.

312 The photodiode provides reference time for the laser
 313 system. The output signal of the photodiode is inverted
 314 and shaped before it is sent to the BAND read-out sys-
 315 tem. The photodiode signal is then digitized by the same
 316 ADCs and TDCs which are used for the PMT signals.

317 2.5. Electronics and DAQ

318 The high voltages for each PMT are provided by a
 319 multi-channel CAEN SYS4527 mainframe with eleven
 320 A1535SN cards with 24 channel each [17, 18].

321 A schematic drawing of the read-out electronics and
 322 its components is shown in Fig. 11. The signal of each
 323 PMT is split to an ADC and TDC, read out independ-
 324 ently. The signal splitters are custom made and have
 325 been used in previous experiments at Jefferson Lab.
 326 From the splitter one signal is sent to a 250-MHz sam-
 327 pling flash-ADCs [19] (FADC) while the other signal

is sent to discriminators. The discriminated time signal goes to a TDC (CAEN VX1190A [20]) with 100-ps resolution per channel.

In total, the system consists of 16 flash-ADCs in one VXS crate, 16 discriminators and two TDCs in a VME crate and 16 splitters. A trigger signal distribution card for the flash-ADCs and trigger interface boards are installed in the crates. All components are part of the standard CLAS12 electronics [21, 22].

The detector is read out either by a trigger from the main CLAS12 trigger system [22] or by stand-alone BAND triggers. The stand-alone triggers are used for tests and calibrations with cosmic rays, radioactive sources and the laser system. They are implemented by a programmable CAEN V1495 logic board [23]. Such triggers include a single bar trigger for source measurements and a coincidence bar trigger for cosmic and laser measurements. The coincidence trigger is also fed to the central CLAS12 trigger system to allow monitoring of the detector by recording laser data during experimental data taking. This laser-monitoring trigger rate is usually about 10 Hz, compared to the $\sim 15 - 20$ kHz trigger rate from electron interactions in the target.

2.6. Final Assembly

Each scintillator bar was assembled and individually tested, following this procedure:

1. Select a pair of matched PMTs.
2. Wrap the assembled scintillator with ESR foil [9], leaving a window-flap for the laser-system optical fiber (see Fig. 10).
3. Glue the PMTs to the light guides with MOMENTIVE RTV615 silicone rubber compound [12].
4. Glue one light guide/PMT assembly to each end of the bar with DYMAX UV curing glue [11].
5. Wrap with light-tight foil^b, leaving a window-flap for attaching the laser-system optical fiber.
6. Glue the optical fiber to the center of the bar and reseal the foil window.
7. Install the mu-metal shields on the PMTs.
8. Search for and fix light leaks by measuring the PMT dark currents with a pico-ammeter.
9. Install each bar in the BAND support frame.
10. Connect the optical fibers and signal and HV cables to patch panels mounted on the upstream side of BAND.

^bBlack 50- μ m thick Tedlar® foil [24] was used to wrap the short bars. The long bars were wrapped with Thorlabs black Aluminium foil [14]

11. Final test for light leaks.

Fig. 12 shows some of the steps in the assembly process, including one bar wrapped with ESR foil, a fully wrapped bar with the optical fiber shown, a row of four bars installed in the BAND frame, and the fully assembled BAND seen from the upstream side with the patch panels for HV, signal cables, and optical fibers.

After assembling the bars in the support frame, the lead wall was installed on the downstream side of BAND. BAND was then craned into its position on top of the central vertex tracker support cart upstream of CLAS12. Fig. 13 shows a design drawing and a photograph of the upstream side of BAND.

Fig. 14 shows the upstream side of BAND in Hall B with about 3/4 of the cables installed. All cables are connected to electronics which is installed outside of the photograph on the left side.

3. Performance

In this section, we first describe the performance of the individual scintillator bars and their calibrations. We next describe the performance of the BAND as a whole, with a focus on neutron identification and efficiency.

3.1. Individual bar performance

3.1.1. Gain matching

In order to have a similar response to a given energy deposit across all PMTs of BAND, each PMT's HV was optimized using cosmic rays. Cosmic ray spectra were measured with a range of HV and then combined to produce a gain curve for each PMT. These data were collected with a cosmic trigger which required a cosmic ray passing through a single vertical layer of BAND to select nearly-vertical cosmic rays. This corresponds to a relatively high energy deposition of 14.2 MeV. For each HV setting we fit the ADC spectrum with a Landau distribution and an exponential background to obtain the cosmic peak position. A representative ADC spectrum is shown in Fig. 15 (top). The obtained gain curve for this PMT is shown in the bottom panel of Fig. 15. The dashed lines indicate the final HV setting to position the cosmic peak at ADC channel 15000. This desired peak position of cosmic rays was chosen to avoid signal overflows in the sampling FADCs for neutron-induced signals, which deposit less energy as compared to cosmic rays. These overflows dominate above ADCs of 20000.

Each PMT gain curve was fit with a power law with parameters α and β

$$ADC = \alpha \cdot \left(\frac{HV}{1500} \right)^\beta, \quad (1)$$

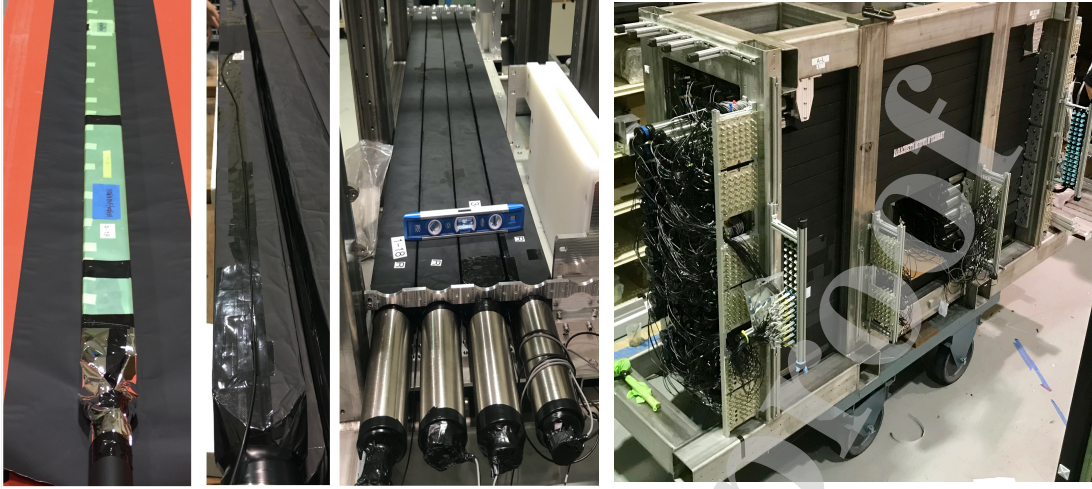


Figure 12: BAND construction. From ESR [9] wrapped bars (left) to assembled detector (right). The intermediate steps show the fully wrapped bars with the optical fiber and the assembled bottom row of the detector.



Figure 13: (left) CAD drawing of the downstream side of BAND and its frame. The lead wall is shown in cyan, the scintillators are in magenta, and the support frame is in black. (right) Photograph of the downstream side of BAND installed in Hall B. The reflective surface in the photograph are the aluminum covers of the lead blocks.

419 where the division by 1500 V was an arbitrary normal- 430
 420 ization to improve fit convergence. The value of the fit 431
 421 parameters for each PMT are shown in Fig. ?? (top). 432
 422 The Hamamatsu R7724 PMTs (red) are more uniform 433
 423 than either of the two ET PMTs, 9954KB (green) or 434
 424 9214KB (blue)^c. However, the cosmic ray ADC peaks 435
 425 are well aligned after adjusting the HV based on the ob- 436
 426 tained gain curves (see bottom panel in Fig. 16). 437

427 3.1.2. Energy deposit calibration 438

428 The ADC response of each PMT is converted to MeV 439
 429 energy deposition by measuring the response to multi- 440

^cWe obtained similar results when using the pulse amplitude of the ADC signal instead of the integral

431 ple radioactive sources and to cosmic rays. The sources 432
 433 ^{60}Co , ^{22}Na , and ^{137}Cs were chosen due to the gamma 434
 435 rays that have Compton edges of 0.963 and 1.118, 436
 437 0.477, and, 1.062 and 0.341, respectively (in MeV). The 438
 439 response to each source was measured in the center of 440
 441 the bar. Using the ADC response to all sources, in com- 442
 443 bination with the attenuation length of the bar, the ADC 444
 445 response can be converted to MeV. These measure- 446
 447 ments were done for a subset of the BAND bars (ones 448
 449 that were accessible following installation) after the bars 450
 451 were gain matched (see previous section). 452

441 A typical response of a PMT to ^{60}Co is shown in 442
 443 Fig. 17 along with a fit of the Compton edge by a 444
 445 parametrization described in [25]. The extracted Comp- 446

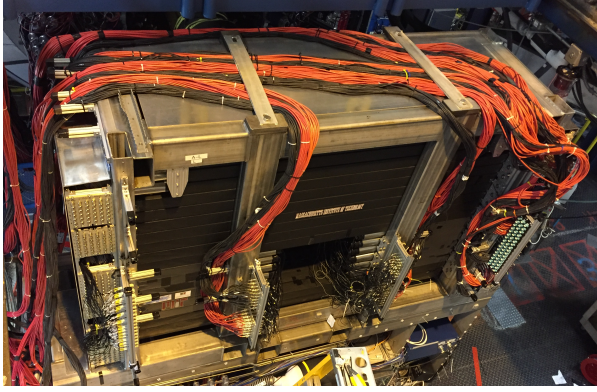


Figure 14: BAND in Hall B. Upstream side with first set of cables installed.

444 ton edges for various bars are quite similar which gives
445 us confidence in applying these measurements to all
446 bars.

447 3.1.3. Time-walk calibration

448 Time-walk calibrations were performed for each
449 PMT with the laser system [4] by using the fiber optic
450 attenuator [16] to vary the amount of light delivered
451 to each bar. Waveforms and times were measured as the
452 attenuator scans from 40 dB to 0 dB. The photodiode
453 output is used as a reference time for any calibrations
454 performed with the laser system, and is external to the
455 variable attenuator.

456 Dependence of a typical PMT time on pulse height
457 is seen in Fig. 18 (left). To correct for time-walk, we
458 parameterize this dependence on the pulse height of the
459 ADC signal, A , as:

$$460 \quad t_{\text{PMT}} - t_{\text{photodiode}} = \alpha + \frac{\beta}{\sqrt{A}}. \quad (2)$$

461 The residual difference, after the time-walk correction,
462 $t_{\text{PMT}} - t_{\text{photodiode}}$, is shown in Fig. 18 (right). At pulse
463 heights close to threshold, the parameterization is not
464 flexible enough and underestimates the strong dependence
465 on pulse height. However, signals with pulse heights this
466 low are not of interest, as we found they are dominated
467 by background, rather than by neutrons (see Section 3.2.3).
468 Any residual corrections that are needed at higher pulse
469 heights are corrected for iteratively, using the same equation
470 as above.

471 3.1.4. Effective velocity

472 The relative time delays between PMTs on the same
473 bar and the speed-of-light in that bar are extracted using
474 cosmic ray data. The effective light speed in a given bar

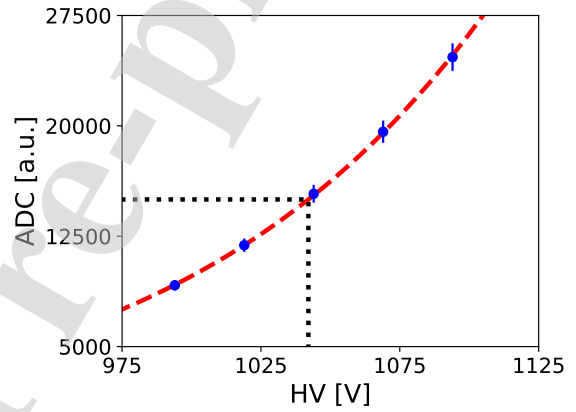
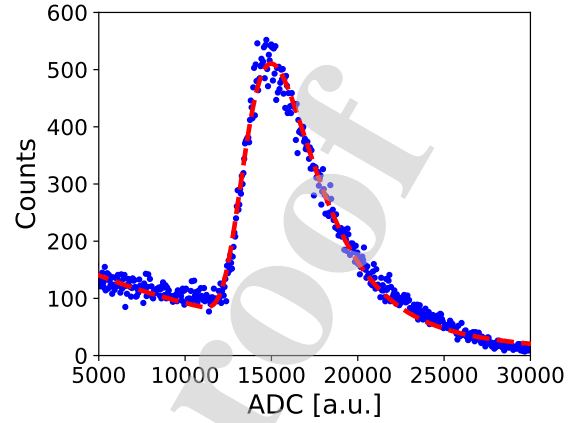


Figure 15: Gain curve measurement. (Top) Typical ADC spectrum for a representative PMT with cosmic rays and the fit with a Landau distribution and an exponential background. (Bottom) Gain curve for the same PMT. The dotted lines indicate the final HV setting to set the cosmic peak to ADC channel 15000.

475 is extracted from the width of the relative timing distribution
476 between its left and right PMTs and the bar's physical length:

$$477 \quad t_L - t_R = -\frac{2x}{v} \quad (3)$$

$$478 \quad -\frac{L}{v} \leq t_L - t_R \leq \frac{L}{v},$$

479 The relative left-right PMT time offset is given by the
480 center of the distribution (see Fig. 19 left). This procedure
481 is done after the PMT timing information has been time-walk
482 corrected. The obtained effective velocities for each bar are
483 shown in Fig. 19 (right) distinguished between short bars (boxes)
484 and long bars (circles). The observed difference is due to geometrical effects from the different bar lengths.

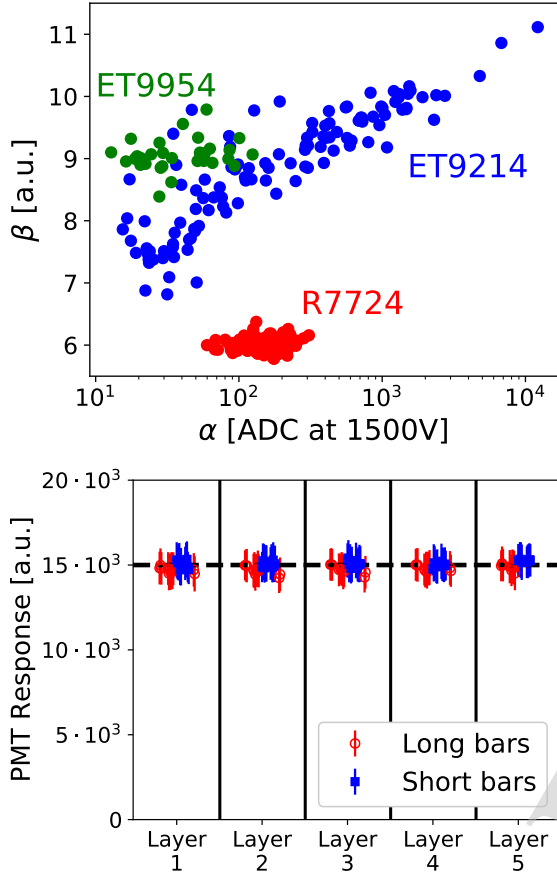


Figure 16: (Top) Gain parameters for each PMT. One sees a greater spread in the Electron Tube PMTs (green and blue) than in the Hamamatsu PMTs (red). (Bottom) $\text{ADC}_{\text{cosmicpeak}}$ position for each bar (vectors not shown) after gain matching. All bars are well aligned.

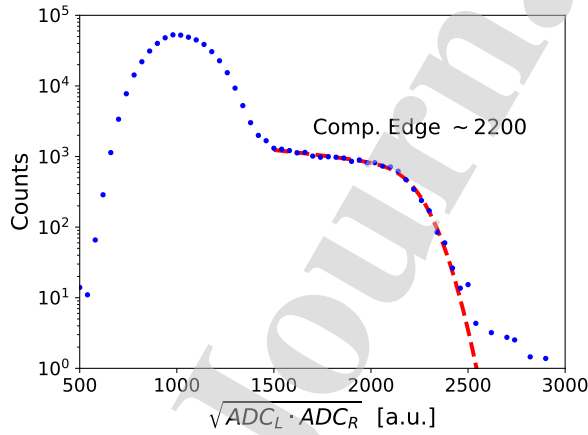


Figure 17: ADC spectrum for a ^{60}Co placed on the center of the bar along with the fit of the Compton edge.

3.1.5. Attenuation length

We measured the effective attenuation length of each completed (assembled and wrapped) bar from cosmic ray data by using the ADC amplitudes (A_L, A_R) and times (t_L, t_R) measured by the two PMTs:

$$\begin{aligned} A_L(x) &= A_0 e^{-\frac{1}{\mu}(L/2-x)} \\ A_R(x) &= A_0 e^{-\frac{1}{\mu}(L/2+x)} \\ R(x) &\equiv \ln \frac{A_L(x)}{A_R(x)} = \frac{2x}{\mu} = \frac{-v(t_L - t_R)}{\mu} \end{aligned} \quad (4)$$

where x is the location of the cosmic-ray hit, μ is the attenuation length, A_0 is the amplitude of cosmic ray interaction, and v is the effective speed of light in the bar. A typical plot of $R(x)$ as a function of $t_L - t_R$ is shown in Fig. 20 (left). We fit the slope of the central part to obtain the attenuation length. The change in slope of the amplitude ratio closer to the edges of the bar is caused by light reflections from the light guides, which affected the amplitude and signal timing for events close to one PMT. We verified this by seeing the reflections in the unintegrated Flash ADC spectrum. We also see this using the integral of the signal (over 80 ns) rather than its amplitude (its peak) for $R(x)$, see Fig. 20 (right). The distribution is linear over the whole bar since most of the reflections are included in the large integration window of 80 ns. However, the attenuation lengths from the integrated signals are very different from the bulk attenuation lengths and those measured in the bench tests due to the multiple reflections.

3.1.6. Individual Bar offsets

After all bars are individually calibrated, relative time delays between bars can still remain, and require correction to combine statistics from all bars. The alignment of all bars can be done quickly using the laser calibration system, as the laser pulse arrival time to each bar should be within the timing resolution. Any residual offset between bars can be corrected later by using the photon arrival time at each bar with respect to electrons detected in the CLAS12 forward detector.

We used the laser calibration system to send light pulses to all the bars. We aligned the average time of each bar, $t_{\text{avg},i} = \frac{1}{2}(t_L + t_R)_i$, with respect to a reference bar in its layer and then we aligned the reference bars to that of layer 5. For example, the alignment for bar i in layer j is done as follows:

$$\begin{aligned} O^{ij} &= \langle t_{\text{avg}}^i - t_{\text{avg}}^j \rangle \\ O^j &= \langle t_{\text{avg}}^j - t_{\text{avg}}^{\text{ref}} \rangle \\ t_{\text{corr}}^{i,j} &= t_{\text{avg}}^i - O^{ij} - O^j, \end{aligned} \quad (5)$$

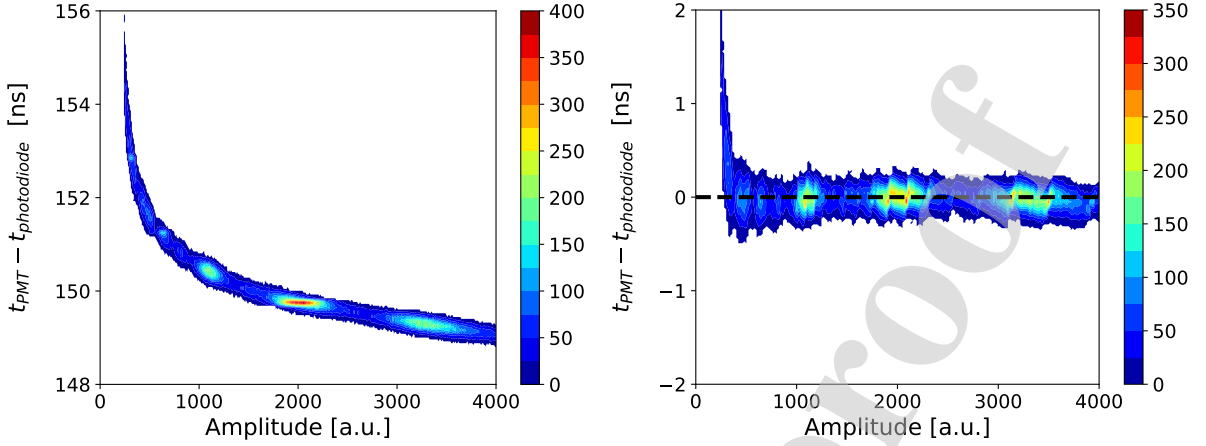


Figure 18: Time-walk calibration: Typical PMT-reference photodiode time difference versus pulse height spectrum for one PMT before time-walk correction (left) and after time-walk correction (right).

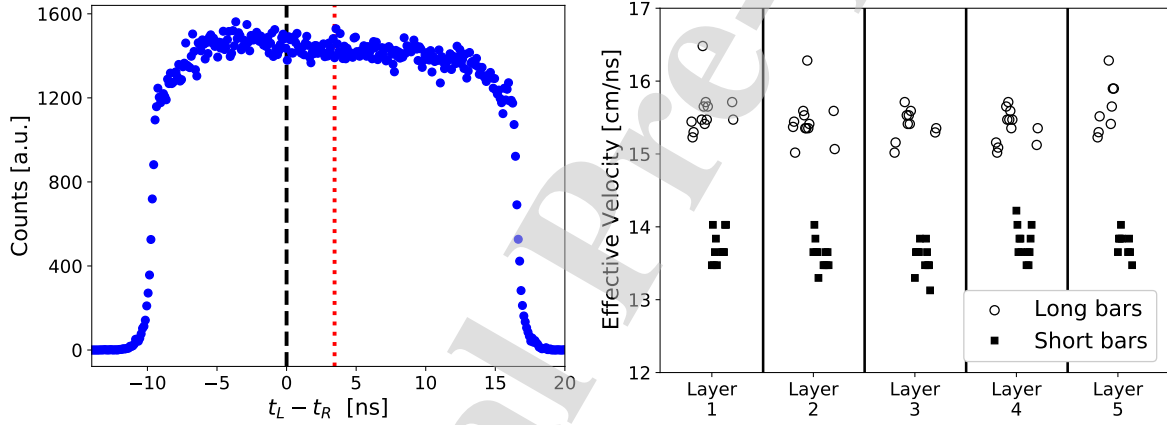


Figure 19: (Left) Typical time-walk corrected $t_L - t_R$ time spectrum in a single bar. The red dotted line indicates the LR offset value from 0. (Right) Effective light-speed for each bar. The differences in effective speeds between long bars (circles) and short bars (boxes) are due to geometrical effects.

525 where t_{avg}^{ref} is the average time of the global reference bar 539
 526 chosen on the most downstream layer of BAND, and t_{avg}^j 540
 527 is the average time of the reference bar chosen in layer 541
 528 j . Then only one global offset is needed to correct the 542
 529 offset of t_{avg}^j if there are no residual offsets between bars. 543

530 3.2. BAND performance

531 3.2.1. Global offset

532 A final global time offset is required to align BAND 546
 533 with CLAS12. The CLAS12 time is determined by the 547
 534 time of the electron detected in the forward detector, as 548
 535 traced back to the target. 549

536 Fig. 21 shows the uncorrected electron-BAND 550
 537 time difference spectrum offset by the photon travel time for 551
 538 each bar. There was a 2-MeV energy deposition cut 552

539 reduce the random coincidence background. The uncor- 540
 541 rected spectrum includes only time walk corrections but 542
 543 no offset corrections. One can see several sharp photon 544
 545 peaks between 50 and 60 ns, far away from the expected 546
 547 zero value. 548

544 After applying the individual offset corrections from 545
 546 the previous section, we determined a timing offset for 547
 548 each bar from the location of its photon timing peak. 549
 550 Applying these offsets results in the corrected spectrum, 551
 552 which displays a well-aligned photon peak with a width of $\sigma = 294$ ps, consistent with the design value. The periodic 4-ns spikes in the remaining spectrum are due to photons correlated with out-of-time electrons from other beam bunches.

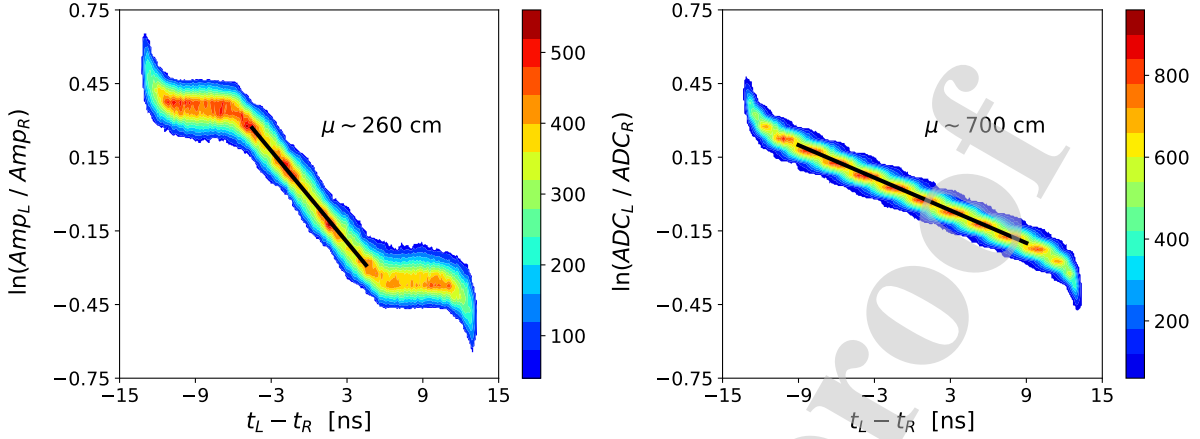


Figure 20: (Left) Log ratio of ADC amplitudes from both PMTs on a bar as a function of time difference of the PMTs. (Right) Log ratio of ADC integral from both PMTs as a function of time difference.

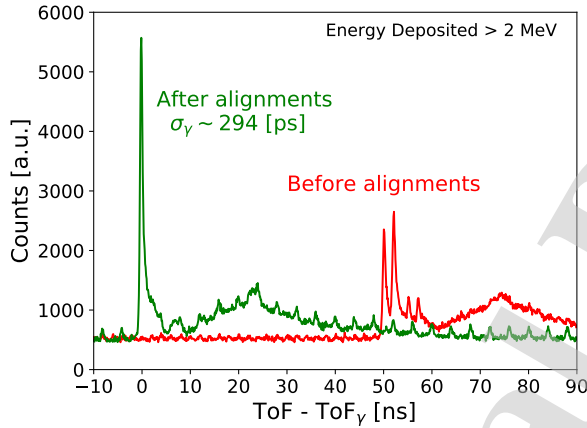


Figure 21: Relative electron-BAND time difference spectrum for all bars offset by the photon travel time for each bar: (red) after time-walk corrections, but not offset corrections, and (green) after all corrections. The bars are well aligned with a width of the photon peak of $\sigma = 294$ ps. A 2-MeV energy deposition cut is applied to reduce the random background. The periodic 4-ns spikes in the remaining spectrum are due to photons correlated with out-of-time electrons from other beam bunches.

3.2.2. Time of Flight resolution

The time resolution of each bar was measured independently using laser calibration data and using the electron-BAND time difference spectrum. The laser data allows us to measure the time resolution over the whole energy deposition range from 0.5 to 7 MeV (see Fig. 7).

The laser-based resolutions are obtained from a Gaussian fit of the difference of the average time of a bar to the reference photodiode as a function of energy de-

posited, see Fig. 22. The resolutions for the 1- and 5-MeV cuts are well below the 300-ps design goal. For the 5-MeV cut, which is a realistic neutron-selection energy deposition cut (see Section 3.2.3) the resolutions are better than 150 ps.

Fig. 22 (right) shows the time resolutions from the measured electron-photon arrival time difference with an energy deposition cut of 2 MeV. We used a high-statistics data run where electrons are detected in CLAS12. The data was also used for the global offset corrections presented in Sec 3.2.1. These measured resolutions include additional uncertainties from the path-length of the target photons to the bar ($\sigma \approx 70$ ps) and from the time resolution of the electron beam bunch ($\sigma \approx 25$ ps). The laser data does not have these uncertainties.

3.2.3. Neutron identification

We identified neutrons from the electron-deuteron, $d(e, e')X$, production data by cutting on the time-of-flight per pathlength (ToF/m), where ToF is the time difference between the time that the electron interacted in the target and the particle arrival time measured by BAND (see Fig. 23 for data with a minimum energy deposition cut of 5 MeV). There are well-separated peaks for photons and for neutrons on top of a flat background from accidental coincidences.

The minimum energy deposition for neutron signals is optimized using the neutron signal-to-background ratio, see Fig. 24. The signal region includes times for neutrons with $200 \leq p_n \leq 600$ MeV/c. The accidental background was estimated by fitting a constant to the left of the photon peak (see Fig. 23). The signal is de-

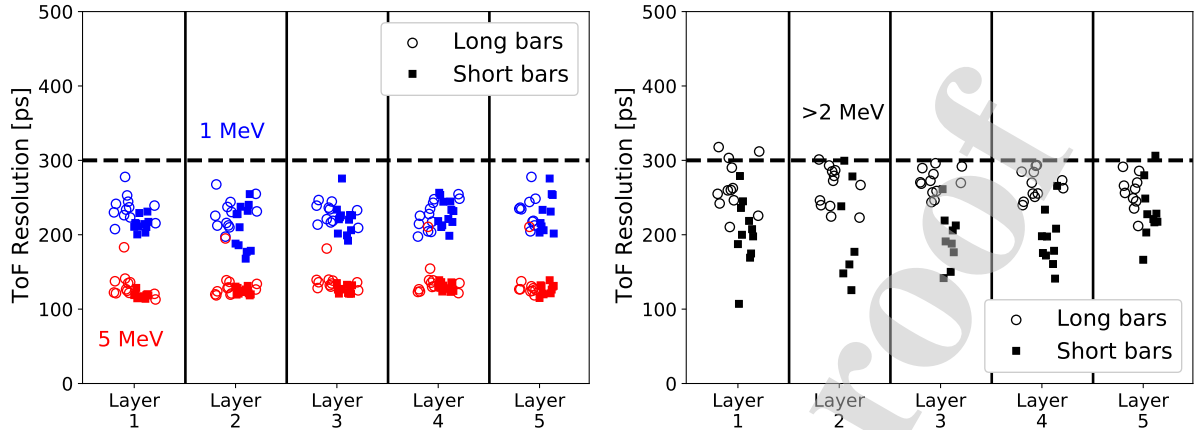


Figure 22: Time resolution for every bar. (Left) as measured with the laser calibration system for two separate energy deposition cuts. (Right) as measured from the electron-photon time difference spectrum with a 2-MeV energy deposition cut. All bars are at or below the required 300-ps resolution.

595 fined as the integral of the spectrum over the signal re-
 596 gion minus the scaled background. As the minimum en-
 597 ergy deposition cut increases, the signal decreases, but
 598 the signal to background ratio increases. With a 5-MeV
 599 energy deposition, the signal-to-background ratio is al-
 600 most three. The optimal cut will be somewhere between
 601 two and seven MeV and will be determined by minimiz-
 ing the experimental uncertainties.

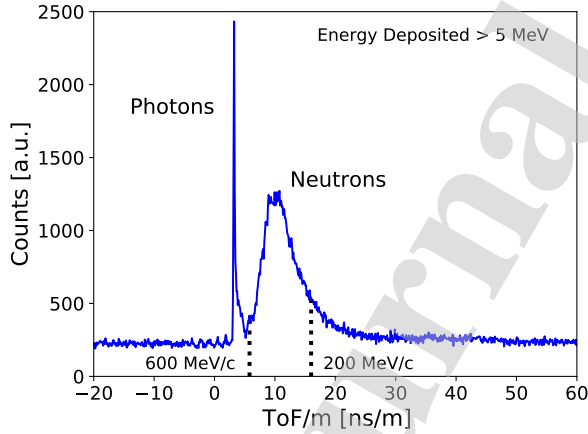


Figure 23: Time-of-flight per meter of BAND hits in coincidence with electrons measured in CLAS12. A sharp photon peak and a broad neutron peak are visible over a flat background from accidentals. The dashed lines indicate the range of neutrons with momenta between 200 and 600 MeV/c.

3.2.4. Neutron efficiency

The efficiency of BAND for neutron detection was studied using a Geant4 simulation, the results of which

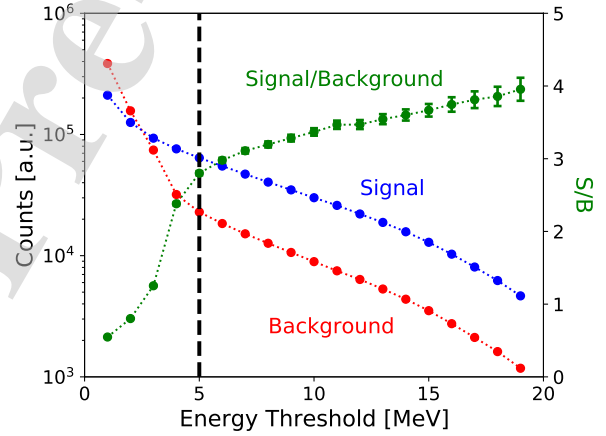


Figure 24: Signal counts (blue) and accidental background counts (red) in the neutron signal region of $200 \leq p_n \leq 600$ MeV/c. The signal-to-background ratio (green) shown with a possible minimum energy deposition cut of 5 MeV.

are shown in Fig. 25. As expected, the efficiency depends both on the energy threshold as well as the neutron momentum.

The Geant4 study did not include the effects of the material between BAND and the CLAS12 target, aside from the lead wall upstream of BAND. Neutrons of different fixed momenta were simulated according to a flat solid-angle distribution, and the efficiency was calculated to be the number of events registering only a single hit with energy deposition above threshold divided by the number of fired neutrons with trajectories hitting BAND. This efficiency is therefore an average over different incident angles and hit positions in BAND. This

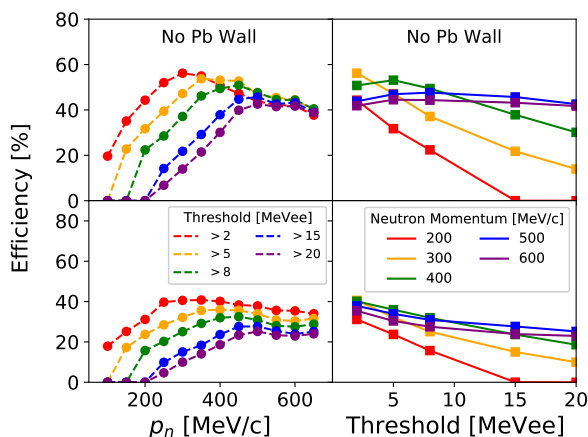


Figure 25: The efficiency of BAND for neutron detection as determined using a Geant4 simulation. (Left) Efficiency as a function of neutron momentum for various energy thresholds, without the effect of the lead wall upstream of BAND (top) and including the lead wall (bottom). (Right) Efficiency as a function of energy threshold for various neutron momenta without the effect of the lead wall upstream of BAND (top) and including the lead wall (bottom).

619 efficiency will be reduced by the effects of neutron multiple scattering in the material between BAND and the CLAS12 target.

622 The simulation indicates that BAND can achieve an efficiency at or above the design goal of above 35% using thresholds between 2- and 5 MeVee, even for higher-momentum neutrons. Running with higher thresholds to suppress background may be possible without significantly compromising BAND's neutron detection efficiency.

629 4. Summary

630 The Backward Angle Neutron Detector (BAND) of CLAS12 detects neutrons emitted at backward angles of 155° to 175° and momenta between 200 and 600 MeV/c. It is positioned 3-m upstream of the target and consists of 18 rows and 5 layers of 7.2-cm by 7.2-cm scintillator bars with PMT readout on both ends to measure time and energy deposition in the scintillator layers. Between the target and BAND there is a 2-cm thick lead wall followed by a 2-cm veto layer to suppress gammas and reject charged particles.

640 Timing calibrations were performed using a novel picosecond-pulsed laser system, along with cosmic and $ed \rightarrow e'n$ data. Energy calibrations utilized a wide range of radioactive sources.

644 After timing and energy calibrations performed, the measured time resolution is below our design goal of

646 300 ps, better than 250 ps (150 ps) for energy depositions above 2 MeV (5 MeV), yielding a momentum reconstruction resolution of $\delta p/p < 1.5\%$.

649 The expected neutron efficiency from simulation is 35%. In the future, we will measure the efficiency using exclusive $ed \rightarrow e'pn$ events collected at Jefferson Lab.

652 Acknowledgements

653 We thank Jefferson Lab's Hall B technical crew for the immense efforts during the BAND assembly, installation, and commissioning, especially Denny Insley, Calvin Mealer and Bob Miller. Thanks to Sergey Boyarinov, Ben Raydo, Chris Cuevas and Armen Stepanyan for providing crucial support in setting up the readout system.

660 We thank Bill Briscoe from George Washington University for generously providing PMTs and voltage dividers for the veto bars. We would like to thank MIT Bates for building the BAND support frame.

664 We also would like to thank Hall B staff for their unwavering support, especially Stepan Stepanyan for setting up an assembly and testing area at Jefferson Lab and Eugene Pasyuk for organizing components. The development of the calibration, reconstruction, and analysis software benefited greatly from discussions, advice, and assistance by Daniel Carman, Raffaella De Vita, and Cole Smith. Finally, thanks to Run Group B of Hall B in Jefferson Lab, and our run-group coordinator, Silvia Niccolai, for their support during data-taking.

674 This work was supported by the U.S. Department of Energy, Office of Science, Office of Nuclear Physics under Award Numbers DE-FG02-94ER40818, DE-SC0020240, DE-FG02-96ER-40960, DE-FG02-93ER40771, and DE-AC05-06OR23177 under which Jefferson Science Associates operates the Thomas Jefferson National Accelerator Facility, the Israel Science Foundation under Grant Nos. 136/12 and 1334/16, the Pazy foundation, the Clore Foundation, and the Chilean FONDECYT grant No. 1201964.

- 684 [1] V. Burkert, et al., The CLAS12 Spectrometer at Jefferson Laboratory, Nucl. Instrum. Meth. A 959 (2020) 163419. doi: 10.1016/j.nima.2020.163419.
- 686 [2] O. Hen, et al., In medium proton structure functions, src, and the emc effect, JLab PAC Proposal (2015). URL <https://misportal.jlab.org/pacProposals/proposals/1159/attachments/93263/E12-11-003A.pdf>
- 688 [3] P. Chatagnon, et al., The CLAS12 Central Neutron Detector, Nucl. Instrum. Meth. A 959 (2020) 163441. doi:10.1016/j.nima.2020.163441.
- 690 [4] A. Denniston, et al., Laser Calibration System for Time of Flight Scintillator Arrays, Nucl. Instrum. Meth. A 973 (2020) 164177. doi:10.1016/j.nima.2020.164177.

- 698 [5] Hamamatsu R7724: [https://www.hamamatsu.com/](https://www.hamamatsu.com/resources/pdf/etd/R7723_R7724_R7725_TPMH1315E.pdf)
699 [resources/pdf/etd/R7723_R7724_R7725_TPMH1315E.](https://www.hamamatsu.com/resources/pdf/etd/R7723_R7724_R7725_TPMH1315E.pdf)
700 [pdf](https://www.hamamatsu.com/resources/pdf/etd/R7723_R7724_R7725_TPMH1315E.pdf).
- 701 [6] ET 9214, [http://et-enterprises.com/products/](http://et-enterprises.com/products/photomultipliers/product/p9214b-series)
702 [photomultipliers/product/p9214b-series](http://et-enterprises.com/products/photomultipliers/product/p9214b-series).
- 703 [7] ET 9954KB, [http://et-enterprises.com/products/](http://et-enterprises.com/products/photomultipliers/product/p9954b-series)
704 [photomultipliers/product/p9954b-series](http://et-enterprises.com/products/photomultipliers/product/p9954b-series).
- 705 [8] BC408 Scintillant: [https://www.](https://www.crystals.saint-gobain.com/sites/imdf.crystals.com/files/documents/bc400-404-408-412-416-data-sheet.pdf)
706 [crystals.saint-gobain.com/sites/](https://www.crystals.saint-gobain.com/sites/imdf.crystals.com/files/documents/bc400-404-408-412-416-data-sheet.pdf)
707 [imdf.crystals.com/files/documents/](https://www.crystals.saint-gobain.com/sites/imdf.crystals.com/files/documents/bc400-404-408-412-416-data-sheet.pdf)
708 [bc400-404-408-412-416-data-sheet.pdf](https://www.crystals.saint-gobain.com/sites/imdf.crystals.com/files/documents/bc400-404-408-412-416-data-sheet.pdf).
- 709 [9] 3M Enhance Specular Reflector: [https://www.3m.](https://www.3m.com/3M/en_US/company-us/all-3m-products/-/3M-Enhanced-Specular-Reflector-3M-ESR-/?N=5002385+3293061534&rt=rud)
710 [com/3M/en_US/company-us/all-3m-products/-/](https://www.3m.com/3M/en_US/company-us/all-3m-products/-/3M-Enhanced-Specular-Reflector-3M-ESR-/?N=5002385+3293061534&rt=rud)
711 [3M-Enhanced-Specular-Reflector-3M-ESR-/?N=](https://www.3m.com/3M/en_US/company-us/all-3m-products/-/3M-Enhanced-Specular-Reflector-3M-ESR-/?N=5002385+3293061534&rt=rud)
712 [5002385+3293061534&rt=rud](https://www.3m.com/3M/en_US/company-us/all-3m-products/-/3M-Enhanced-Specular-Reflector-3M-ESR-/?N=5002385+3293061534&rt=rud).
- 713 [10] Overview over Hamamatsu PMTs: [https://www.](https://www.hamamatsu.com/resources/pdf/etd/High_energy_PMT_TPMZ0003E.pdf)
714 [hamamatsu.com/resources/pdf/etd/High_energy_](https://www.hamamatsu.com/resources/pdf/etd/High_energy_PMT_TPMZ0003E.pdf)
715 [PMT_TPMZ0003E.pdf](https://www.hamamatsu.com/resources/pdf/etd/High_energy_PMT_TPMZ0003E.pdf).
- 716 [11] DYNAMAX Ultra Light-Weld 3-20262, [http://www.dymax.](http://www.dymax.com/images/pdf/pds/3-20262.pdf)
717 [com/images/pdf/pds/3-20262.pdf](http://www.dymax.com/images/pdf/pds/3-20262.pdf).
- 718 [12] MOMENTIVE RTV615 silicone rubber compound, [https:](https://www.momentive.com/en-us//products/tds/rtv615?productId=64616a84-08ff-4372-a2a2-a58eb45be627)
719 [//www.momentive.com/en-us//products/tds/rtv615?](https://www.momentive.com/en-us//products/tds/rtv615?productId=64616a84-08ff-4372-a2a2-a58eb45be627)
720 [productId=64616a84-08ff-4372-a2a2-a58eb45be627](https://www.momentive.com/en-us//products/tds/rtv615?productId=64616a84-08ff-4372-a2a2-a58eb45be627).
- 721 [13] R. Fair, et al., The CLAS12 superconducting magnets, Nucl.
722 *Instrum. Meth. A* 962 (2020) 163578. doi:10.1016/j.nima.
723 2020.163578.
- 724 [14] Thorlabs black Aluminium foil, [https://www.thorlabs.](https://www.thorlabs.com/thorproduct.cfm?partnumber=BKF12)
725 [com/thorproduct.cfm?partnumber=BKF12](https://www.thorlabs.com/thorproduct.cfm?partnumber=BKF12).
- 726 [15] Teem Photonics: [https://www.teemphotonics.com/](https://www.teemphotonics.com/laser/microchip-laser-355-nm-1e-4khz-600ps)
727 [laser/microchip-laser-355-nm-1e-4khz-600ps](https://www.teemphotonics.com/laser/microchip-laser-355-nm-1e-4khz-600ps).
- 728 [16] OZ Optics: [https://www.ozoptics.com/products/](https://www.ozoptics.com/products/attenuators.html)
729 [attenuators.html](https://www.ozoptics.com/products/attenuators.html).
- 730 [17] CAEN SY4527: [https://www.caen.it/products/](https://www.caen.it/products/sy4527/)
731 [sy4527/](https://www.caen.it/products/sy4527/).
- 732 [18] CAEN A1535SN: [http://www.caen-group.com/](http://www.caen-group.com/servlet/checkCaenManualFile?Id=9315)
733 [servlet/checkCaenManualFile?Id=9315](http://www.caen-group.com/servlet/checkCaenManualFile?Id=9315).
- 734 [19] JLab 250 MHz FADC manual.
735 URL [https://www.jlab.org/Hall-B/ftof/manuals/](https://www.jlab.org/Hall-B/ftof/manuals/FADC250UsersManual.pdf)
736 [FADC250UsersManual.pdf](https://www.jlab.org/Hall-B/ftof/manuals/FADC250UsersManual.pdf)
- 737 [20] CAEN VX1190A: [https://www.caen.it/products/](https://www.caen.it/products/v1190a-2esst/)
738 [v1190a-2esst/](https://www.caen.it/products/v1190a-2esst/).
- 739 [21] S. Boyarinov, et al., The CLAS12 Data Acquisition System,
740 *Nucl. Instrum. Meth. A* 966 (2020) 163698. doi:10.1016/
741 *j.nima.2020.163698*.
- 742 [22] B. Raydo, et al., The CLAS12 Trigger System, *Nucl. Instrum.*
743 *Meth. A* 960 (2020) 163529. doi:10.1016/j.nima.2020.
744 163529.
- 745 [23] CAEN V1495: <https://www.caen.it/products/v1495/>.
- 746 [24] Dupont Tedlar foil, [https://www.dupont.com/](https://www.dupont.com/content/dam/dupont/products-and-services/membranes-and-films/pvf-films/documents/DEC_Tedlar_GeneralProperties.pdf)
747 [content/dam/dupont/products-and-services/](https://www.dupont.com/content/dam/dupont/products-and-services/membranes-and-films/pvf-films/documents/DEC_Tedlar_GeneralProperties.pdf)
748 [membranes-and-films/pvf-films/documents/DEC_](https://www.dupont.com/content/dam/dupont/products-and-services/membranes-and-films/pvf-films/documents/DEC_Tedlar_GeneralProperties.pdf)
749 [Tedlar_GeneralProperties.pdf](https://www.dupont.com/content/dam/dupont/products-and-services/membranes-and-films/pvf-films/documents/DEC_Tedlar_GeneralProperties.pdf).
- 750 [25] M. J. Safari, F. Abbasi Davani, H. Afarideh, Differentiation
751 method for localization of Compton edge in organic scintilla-
752 tion detectors arXiv:1610.09185.